Advanced Electronic Materials

ADVANCED ELECTRONIC MATERIALS Open Access

www.advelectronicmat.de

RESEARCH ARTICLE OPEN ACCESS

Thin-Film Thermal Sensors on Chitosan Substrates for Sustainable Transient Electronics

Ahmed Rasheed[1,2] | Soufiane Krik[1] | Sundus Riaz[1] | Hafiza Faiqa Maqsood[1] | Jacopo Nicoletti[3] | Riccardo Zamboni[1] | Guglielmo Trentini[1,4] | Pietro Ibba[1] | Franco Cacialli[1,2] | Andrea Gaiardo[4] | Giuseppe Cantarella[5] | Niko Münzenrieder[1,3] | Paolo Lugli[1,2] | Giovanni Antonio Salvatore[3] | Luisa Petti[1]

[1]Faculty of Engineering, Free University of Bozen-Bolzano, Bolzano, Italy | [2]Competence Centre for Mountain Innovation Ecosystems, Piazzetta Franz Innerhofer, 8, Free University of Bozen-Bolzano, Bolzano, Italy | [3]Department of Molecular Sciences and Nanosystems, Ca'Foscari University of Venice, Venice, Italy | [4]Fondazione Bruno Kessler (FBK), Trento, Italy | [5]Department of Physics, Informatics and Mathematics, University of Modena and Reggio Emilia, Modena, Italy

Correspondence: Ahmed Rasheed (Ahmed.Rasheed@unibz.it)

Received: 4 October 2025 | **Revised:** 16 January 2026 | **Accepted:** 6 February 2026

Keywords: chitosan film | flexible sensors | thin film sensors | transient electronics | transient | wearable devices

ABSTRACT

In recent years, transient (bio)electronics has witnessed a remarkable surge for their potential in sustainable and biocompatible electronic solutions. Here, chitosan-based films are demonstrated as versatile transient substrates for thin-film thermal sensors, merging sustainability with standard microfabrication. Two sensor types are fabricated: resistive temperature detectors (RTDs) via sputtering of a 100 nm molybdenum (Mo) layer, and thermistors through subsequent deposition of a 50 nm amorphous indium gallium zinc oxide (a-IGZO) semiconductor layer. Bi-directional thermal characterization in physiologically relevant ranges (25–55 °C, < 2.0% RH) reveals that both device types exhibited linear and reproducible responses. The thermistors show a significantly higher sensitivity (0.0184 $°C^{-1}$) more than an order of magnitude greater than the RTDs (0.0010 $°C^{-1}$), with minimal deviation during extended thermal cycling (standard deviations < ~0.016 $°C^{-1}$ and < ~0.0006$°C^{-1}$, respectively). The sensors maintain full functionality under severe mechanical deformation, including twisting, folding, and bending to radii as small as 8 mm. Importantly, the devices are fully transient, dissolving completely in aqueous and mildly acidic environments within approximately 50 hours. This work establishes chitosan-based substrates as a promising platform for functional transient electronics leveraging existing thin-film technologies, paving the way for sustainable applications in soft robotics, agritech, and healthcare.

1 | Introduction

Conventional electronics have become essential to modern life, powering technologies from computing to communications. But their growing use has also created major sustainability challenges, particularly the rapid rise of electronic waste (e-waste). In 2022, global e-waste reached 62 million tonnes (MT), and it is expected to grow by 32% to 82 MT by 2030 [1, 2]. This e-waste contains valuable resources, including about 31 MT of metals, 17 MT of plastics, and 14 MT of other materials. However, recovery is inefficient, especially for precious metals and rare earth elements, which were valued at roughly USD 57 billion in 2019 [1]. In addition, the energy-intensive production of conventional devices further depletes resources and increases CO_2 emissions.

In this context, flexible and thin-film electronics offer a promising way to address these challenges, especially when designed with sustainability in mind. These devices, while not matching the electrical performance of rigid electronics, are lightweight,

adaptable, and can even be transient, offering unique advantages and new functionalities. These properties make them well suited for applications where permanent devices are unnecessary or undesirable, e.g., in soft robotics, wearables, agritech, and more generally Internet of Things (IoT) applications [3–8].

These devices typically combine flexible substrate with functional thin films of conductive, semiconductive, and insulating materials, each carefully designed to maintain performance while preserving flexibility and adaptability [9, 10]. Building on this, one effective way to improve the sustainability of flexible electronics is to use renewable and responsibly sourced materials. This contrasts with the common use of conventional polymers, such as polydimethylsiloxane (PDMS) [11], polyimide (PI) [12–15], polyethylene terephthalate (PET) [16, 17], polyethylene naphthalate (PEN) [18, 19], and polyetheretherketone (PEEK) [20], which are typically non-renewable and not easily degradable/dissolvable. Bioderived substrates offer inherent advantages due to their biocompatibility and biodegradability. This class of materials includes fibroin protein like silk [21] and gelatin [22], and polysaccharides such as cellulose [23], chitin [24], chitosan [25], and starch [26].

Among the available options, chitosan a natural biopolymer derived from chitin is particularly attractive. It is the second most abundant polysaccharide on Earth [27, 28], and its cost-effectiveness is supported by the annual European production of crustacean shell waste, which amounts to roughly 750000 tons [29]. Assuming a 20% extraction efficiency, this waste could yield approximately 150 000 tons of chitin and chitosan per year [30, 31], aligning well with eco-friendly acquisition and processing practices [32].

Chitosan offers a range of valuable properties, including biocompatibility, non-toxicity, biodegradability [33, 34], antiviral and antibacterial activity [35], and excellent film-forming ability [36]. These characteristics make chitosan films suitable for biomedical applications such as tissue engineering [37], e-skin devices [38], and wound healing [39], as well as for industrial uses including optical [40, 41] and humidity sensors [42]. While chitosan substrates have been explored for various electronic devices, the development of high-performance thin-film thermal sensors on this platform remains unreported. This work addresses this gap by introducing fully transient temperature sensors fabricated on pristine chitosan, leveraging chitosan inherent properties and enabling a green end-of-life, dissolving completely in aqueous environments and aligning with the goal of zero-waste creation.

This work presents flexible thin-film temperature sensors built entirely from transient materials on chitosan substrates, chosen for its biocompatibility and biodegradability. Characterization of the solution-processed chitosan films shows high transparency (>90%) and Young's modulus of 750 MPa, sustaining elastic deformation up to 10% strain.

Two sensor architectures were fabricated via sputtering deposition: a resistance temperature detector (RTD) with a molybdenum (Mo) layer, and a thermistor based on a Mo/amorphous indium-gallium-zinc-oxide (Mo/a-IGZO) structure.Sensor performance was characterized in the physiological temperature window of 25 °C to 55 °C, which was selected to encompass ambient conditions, physiological skin temperatures, and moderate thermal stress levels relevant to epidermal and plant-interface sensing, while remaining below the thermal softening and degradation regimes of chitosan [43, 44]. The thermistor exhibited a high sensitivity of –0.0182 $°C^{-1}$, while the RTD showed a lower sensitivity of 0.0010 $°C^{-1}$ but negligible hysteresis. Both devices maintained stable performance over repeated temperature and humidity cycling.

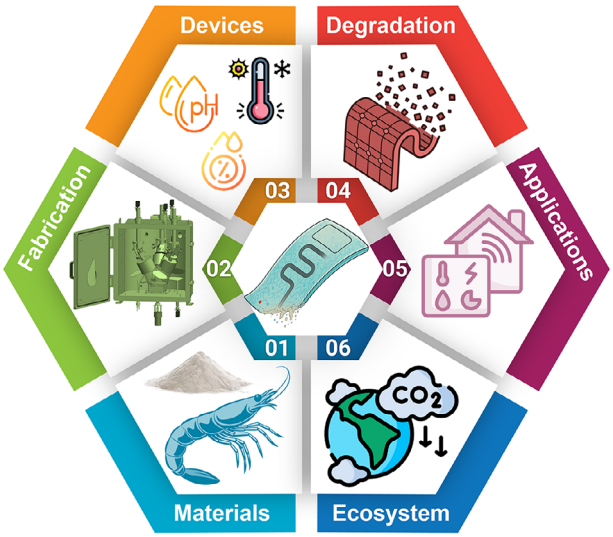

FIGURE 1 | Schematic overview of this work, highlighting the key aspects of sustainable electronics development. A chitosan film derived from natural polymers serves as the substrate, onto which thermal sensors with positive and negative temperature coefficients are fabricated via dry magnetron sputtering. These devices are dissolvable and environmentally friendly, generating no persistent e-waste.

Dissolution tests in deionized water, lime solution, and edible vinegar confirmed that chitosan films, RTDs, and thermistors fully dissolve in less than 50 hours. These results demonstrate that chitosan-based substrates provide a natural and sustainable platform for transient electronics, enabling devices that function effectively while leaving no persistent e-waste. Figure 1 presents the conceptual design of the transient thin-film sensing devices developed in this work.

2 | Results and Discussion

2.1 | Preparation and Characterization of Chitosan Films

Figure 2 shows a schematic of the fabrication process for the chitosan films. Initially, a stable and homogeneous chitosan (CS) solution was prepared by dissolving CS powder in acetic acid, followed by stirring and sonication. The film was then fabricated via solution casting onto a selected carrier (e.g., polyimide or glass) using an automatic applicator. The cast film was dried overnight by solvent evaporation, after which it could be peeled off. Details of the fabrication process are provided in the Experimental Section. Figure 2 illustrates the resulting chitosan films, showing their thin, lightweight and transparent nature as free-standing 2(i), on Kapton foil 2(ii), and on a glass carrier 2(iii).

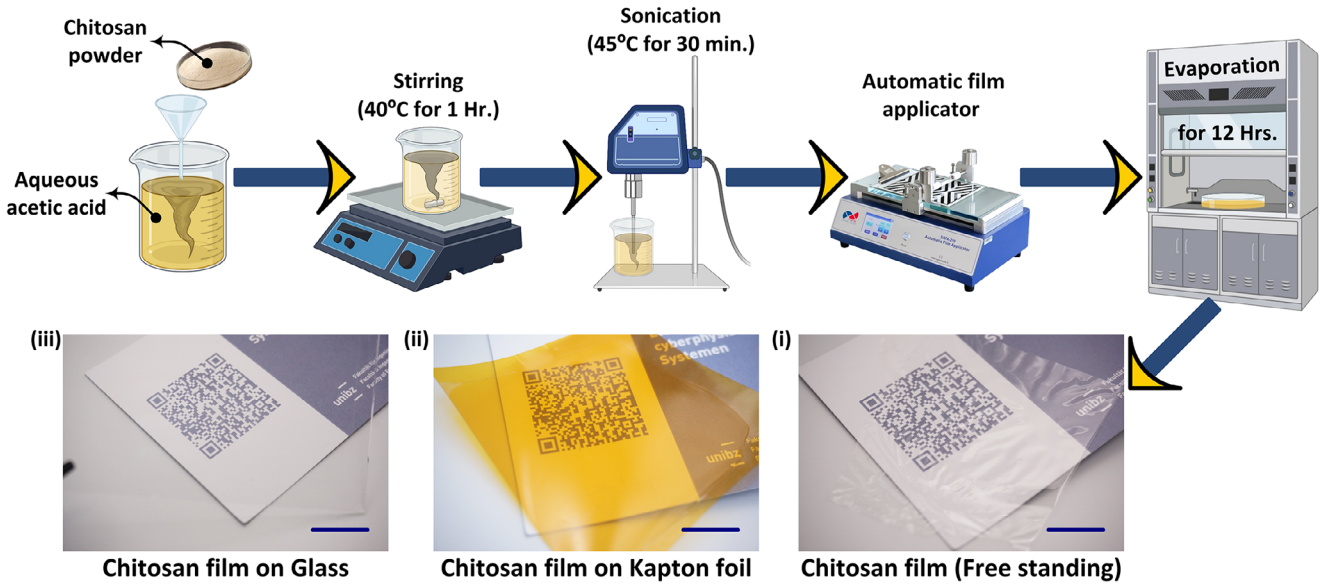

FIGURE 2 | Fabrication process and characteristics of chitosan films. Schematic of the solution casting process, where a chitosan-acetic acid solution is stirred, sonicated, cast using a film applicator, and dried to form a solid film. Digital photographs demonstrating the film's versatility as (i) free-standing membrane (scale bar: 10 mm) or (ii) coated on Kapton foil (scale bar: 10 mm) and (iii) glass substrates (scale bar: 10 mm).

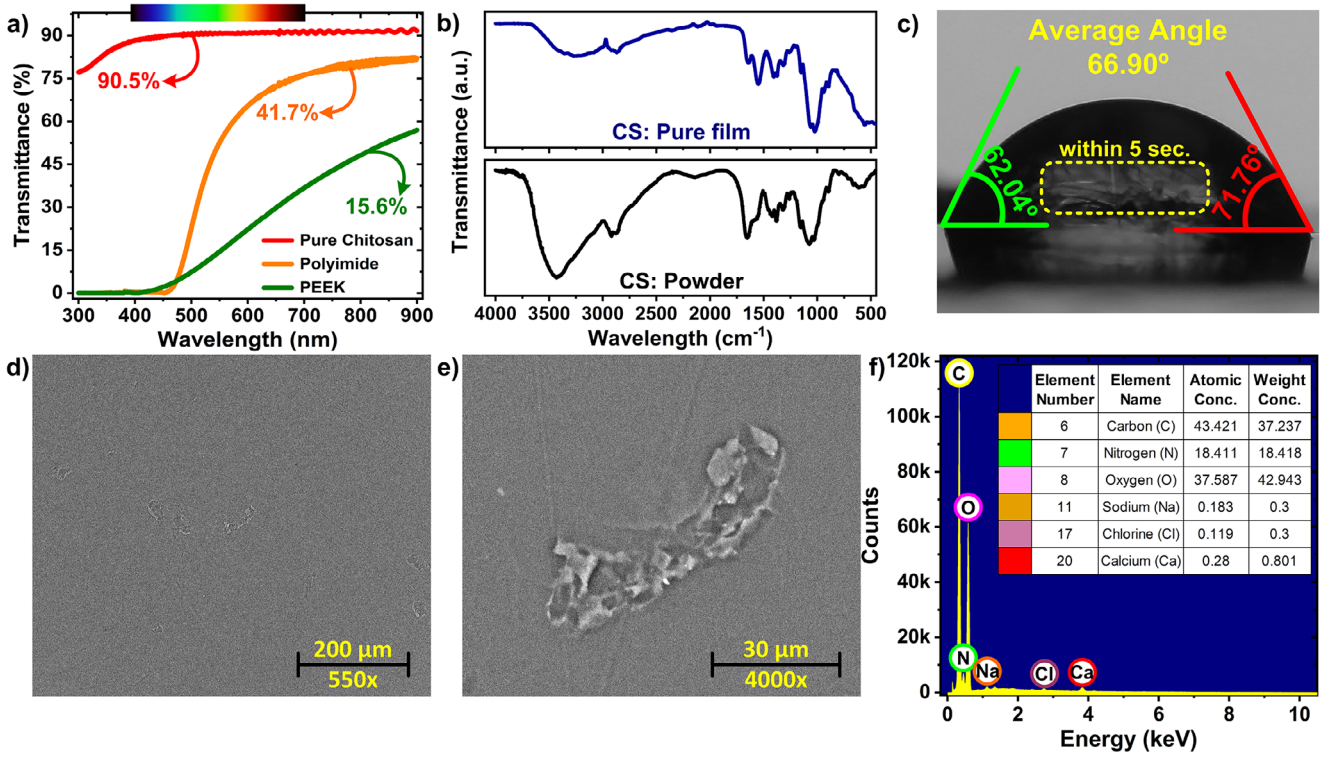

FIGURE 3 | Optical, structural, and surface characterization of chitosan and reference films. (a) Transmittance spectra of 50-µm-thick pure chitosan (CS) film, 50-µm-thick PEEK, and 50-µm-thick polyimide. (b) FTIR spectra of chitosan (CS) powder and pure chitosan film. (c) Water contact angle measurement on the pure chitosan film. (d, e) FESEM images of pure chitosan films at different magnifications. (f) Elemental mapping of the pure chitosan film.

The thickness of the resulting chitosan film was measured to be approximately ~50-µm using a stylus profilometer. Figure 3a compares the transmittance spectra of the pure chitosan film with two commonly used flexible electronic substrates: polyetheretherketone (PEEK) and polyimide (Kapton1E, DuPont), both with similar thicknesses of 50 µm. The chitosan film exhibits a high optical transmittance of 90.5% in the visible range (400–700 nm, upper inset), significantly surpassing the transmittance values of 41.7% for polyimide and 15.6% for PEEK. This superior transparency highlights the potential of chitosan

films for imperceptible, transparent, and unobtrusive electronic applications.

Fourier-transform infrared (FTIR) spectroscopy was employed to analyze the chemical and aggregated structure of the chitosan film relative to chitosan powder, with the resulting spectra shown in Figure 3b. The spectrum exhibits all characteristic vibrational peaks of chitosan: a broad band at 3250–3500 cm^{-1} corresponding to overlapping O–H stretching and N–H deformation, a band at 2850–2970 cm^{-1} associated with C–H stretching, a peak at 1652 cm^{-1} attributed to C = O stretching of the amide I group, a peak at 1555 cm^{-1} corresponding to N–H angular deformation of the amide II group, a peak at 1319 cm^{-1} related to C = O–NH_2 axial deformation of the amide III group, and finally a peak at 1047 cm^{-1} corresponding to C–O angular deformation of chitosan. The retention of these functional groups indicates that the film fabrication process did not alter the chemical integrity of chitosan.

X-ray diffraction (XRD) measurements for the fabricated chitosan films used in this study exhibit patterns similar to those reported previously [25], confirming that the films are substantially amorphous. This amorphous structure, resulting from the solution-casting process, typically leads to a weak intrinsic piezoelectric response in such materials. In amorphous thin films lacking dipolar orientation, any potential piezoelectric contribution is further suppressed [45]. The amorphous nature nevertheless contributes to the films' high optical transparency and influences their thermomechanical properties, including the glass transition and softening behavior discussed subsequently.

Surface wettability was quantified by water contact angle measurements on the film surface. Sessile water droplets (~2 μL) were deposited on the film surface using a syringe, yielding an average initial contact angle of 66.9° as shown in Figure 3c. This acute angle confirms the strongly hydrophilic nature of the chitosan surface. Subsequent to deposition, rapid capillary infiltration and polymer network swelling occurred, causing the liquid to spread and penetrate the film within seconds. This early-stage absorption and interpenetration, visible within 5 s, is highlighted in the yellow dashed rectangle of Figure 3c, and complete droplet dispersion was observed within minutes (Figure S2, Supporting Information), further confirming the high wettability of the chitosan film.

Surface morphology characterization via scanning electron microscopy (SEM) at 550× and 4000× magnifications, shown in Figure 3d,e, revealed a generally smooth, flat, and uniform surface with only a few localized protrusions, indicating an overall homogeneous particle distribution. Height mapping and first-order planarization of a representative protrusion (Figure S3, Supporting Information) showed an arithmetical mean height (S_a) on the order of hundreds of nanometers. Finally, energy-dispersive X-ray spectroscopy (EDX) elemental mapping confirmed the presence of carbon, nitrogen, and oxygen in the pristine film (Figure 3f), consistent with the expected chitosan composition.

To address the dielectric properties of the chitosan substrate, electrochemical impedance spectroscopy was performed as a function of frequency (1 Hz–1 MHz) and temperature (303-327 K). Both the real (ε_1) and imaginary (ε_2) parts of the permittivity exhibit a pronounced low-frequency increase, consistent with electrolyte-like behavior arising from interfacial polarization and ionic transport within the biopolymer matrix. At 1 Hz and at ambient temperature, the real part of the permittivity is approximately $\varepsilon_r \approx 2.5$, which is in good agreement with reported values for thin chitosan films [46, 47]. This value is comparable to commonly used flexible polymeric substrates such as polyimide ($\varepsilon_r \approx 3$–3.6) [43, 44], confirming the suitability of chitosan for electronic applications beyond the resistive temperature sensors demonstrated here. The temperature dependence of the dielectric response further supports the ionic polarization mechanism. The frequency- and temperature-dependent dielectric characteristics are summarized in Figure S4 (Supporting Information), providing a relevant reference for future system-level and wireless device implementations.

Moreover, the mechanical behavior of the chitosan substrate is strongly temperature-dependent, governed by polymer chain mobility and intermolecular hydrogen bonding [48]. Within the range investigated in this work, the substrate remains mechanically stable, enabling reliable sensor operation. At room temperature, the thin substrate film remains flexible and mechanically compliant, enabling stable integration of RTD and thermistor structures without cracking or delamination. With increasing temperature, gradual softening is observed above ~65 °C, due to thermally activated chain relaxation and partial disruption of hydrogen-bond networks within the polysaccharide matrix [49, 50]. While chitosan undergoes chemical degradation only at substantially higher temperatures (>200 °C), mechanical stability and dimensional fidelity of thin films can be compromised at lower temperatures due to moisture loss and weakened physical crosslinks. Accordingly, an operational temperature window of approximately <65 °C is defined for mechanically stable device performance, fully encompassing the low- to moderate-temperature sensing applications demonstrated here, whereas for the glass carrier supported chitosan films, constrained from deformations by strong interfacial adhesion, remain stable up to ~80 °C.

2.2 | Fabrication and Characterization of Thin-Film Thermal Sensors

The chitosan substrates were air-cleaned prior to fabricating mono-layered resistive temperature detectors (RTDs) and bi-layered thermistors. Among degradable metals such as Zn, Mg, Fe, Mo, and W, molybdenum (Mo) was chosen due to its superior electrical conductivity for efficient charge transfer, excellent thermal properties for heat dissipation, high mechanical endurance under stress, and environmentally benign biodegradation profile.The optimized deposition pressure during sputtering process was selected to ensure both the electrical quality of the Mo layer and its mechanical adhesion to the chitosan substrate. While lower pressures can increase film density, they induce high stress leading to poor adhesion and micro-cracks on flexible surfaces. Before device fabrication, the sheet resistance of the deposited material layers was characterized. Test structures consisting of rectangular stripes (7 mm (W) × 22 mm (L)) were used to measure the sheet resistance of sputtered Mo on the chitosan film. The linear I–V characteristics confirm good ohmic contact, and measurements acquired at different locations across the samples

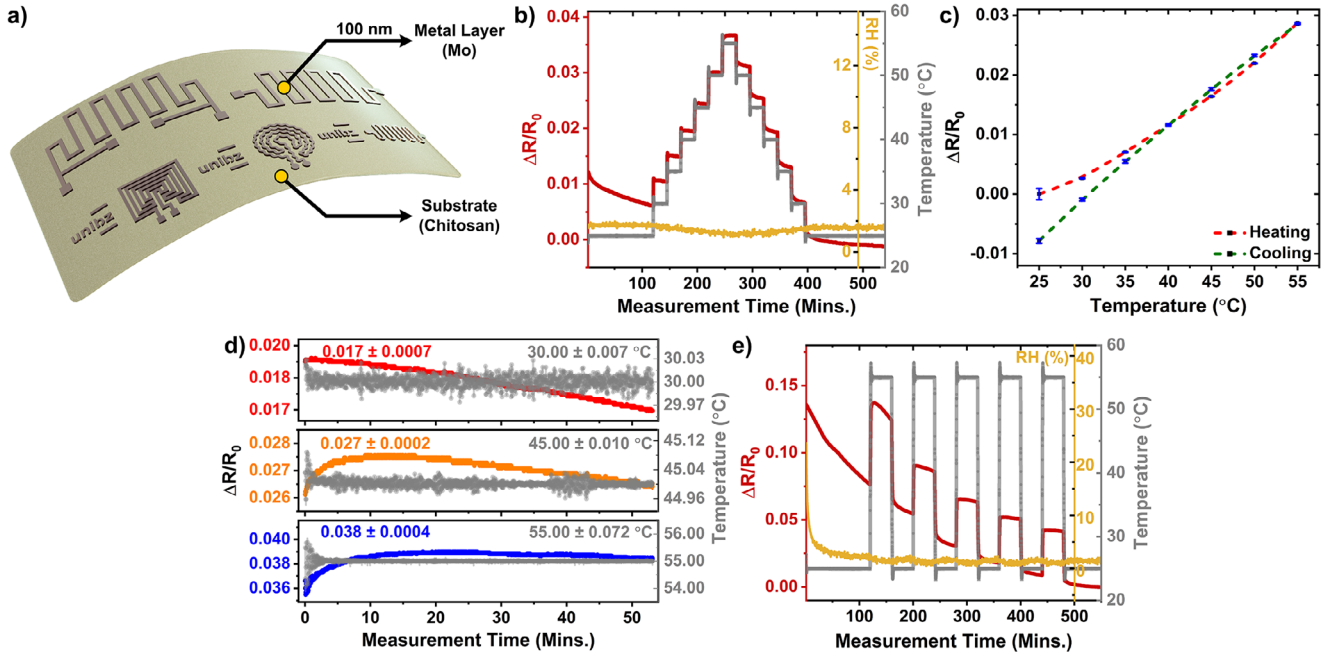

FIGURE 4 | Characterization and performance evaluation of the Mo-based resistive temperature detector (RTD) fabricated on a chitosan substrate. (a) 2D schematic illustration of the RTDs. (b, c) Relative change in resistance as a function of temperature in a bi-directional sweep between 25 °C and 55 °C. (d) Stability test of the RTD by monitoring resistance for approximately 1 h at 30 °C, 45 °C, and 55 °C. (e) Cyclic measurements from 25 °C to 55 °C performed five times to evaluate the sensor's reliability.

indicate stable sheet resistance values of 80.13 ± 0.02 Ω/sq. for the Mo layer (Figure S5a,b, Supporting Information) The complete fabrication procedures for the RTD and thermistor sensors are detailed in the Experimental Section. Figures 4a presents schematic diagrams of the RTD configurations, while Figure S6a,b (Supporting Information) displays the fabricated devices on flexible pure chitosan films (~50 μm-thick). Representative optical micrographs of a serpentine resistive temperature sensor are shown in Figure S6c,d (Supporting Information).

The thermal performance of the RTDs was characterized using a custom-built setup (see Experimental Section).The presented data corresponds to a representative device, while a total of four devices were characterized. Heating and cooling curves for the remaining RTDs, along with their corresponding temperature coefficients, are shown in Figure S9a,b (Supporting Information), with device-to-device variations. Each data point represents the response of independently fabricated RTD devices, with error bars indicating the standard deviation, while corresponding TCR values are extracted from the linear fits. Devices were evaluated over a biologically relevant range of 25 °C and 55 °C in 5 °C increments under controlled humidity (<2%). At each temperature step, the sensors were stabilized for 20 minutes, with additional pre- and post-measurement stabilization periods of 120-minute at 25 °C to ensure data reliability. Figure 4b,c shows the ramp-up and ramp-down responses, illustrating the relative resistance change of the Mo-based RTDs during heating and subsequent cooling. The sensors exhibited predominantly linear and stable behavior across the examined range, with only a minor deviation of less than 0.01 in relative resistance observed at 25 °C. The temperature coefficient of resistance (TCR, α) was calculated from the slope of the resistance-temperature curve i.e., $\alpha = (R - R_0)/[R_0(T - T_0)]$, yielding values of $0.0010\,°C^{-1}$ during heating and $0.0011\,°C^{-1}$ during cooling. The small hysteresis observed is likely attributable to induced thermal strain within the chitosan film or gradual annealing of the Mo electrodes. Notably, reduced drift in the post-cooling stabilization phase compared to the pre-heating phase suggests improved device stability, reduced hysteresis, and a more consistent α value after thermal cycling. Quantitative analysis of the temperature steps within the thermal characterization reveals consistent dynamic performance. The sensor's response time to a heating step (e.g., from 25 °C to 30 °C, from 30 °C to 35 °C and from 50 °C to 55 °C) is approximately 12 seconds, while the recovery time upon cooling for the same temperature ranges is approximately 19 seconds. These rapid response and recovery kinetics, which remain consistent across various setpoint intervals, highlight the sensor's excellent thermal agility.

The RTD's reliability was further assessed through extended exposure to set temperatures as shown in Figure 4d. The RTDs were held at 30 °C, 45 °C, and 55 °C for approximately one hour each, maintaining relative resistance values of 0.017±0.0007, 0.027±0.0002, and 0.038±0.0004, respectively.The observed drift in the initial phase at near-ambient temperatures could be due to the minor environmental variations, e.g., humidity-induced swelling and thermal equilibration, whereas at higher temperatures (45 °C and 55 °C) the larger resistance change improves the signal-to-noise ratio and suppresses apparent drift. Importantly, the variation at 30 °C remains limited to ±0.0007 (≈ 4% of the signal) and non-monotonic, indicating no permanent degradation, and thus has a negligible impact on the overall accuracy and reliability of the RTD. Cyclic stability tests, comprising five heating-cooling cycles between 25 °C and 55 °C, each with a 30 minute dwell time as shown in Figure 4e, revealed a significant shift in baseline resistance at the first cycle. This initial variation

is attributed to a thermal expansion mismatch between the electrode and substrate upon first exposure to elevated temperature alongside the settling of relative humidity from ∼35% down to less than ∼2%. However, the response profile exhibited consistent magnitude and shape across subsequent cycles, indicating robust operational stability after this initial conditioning.In addition, ambient storage stability was evaluated by tracking the resistance of a representative RTD over three months, which showed a normalized change of only $\Delta R/R_0 \approx 1.6\%$ (from 1.93 kΩ to 1.96 kΩ), confirming good chemical and interfacial stability of the Mo layer on the chitosan substrate.Finally, the ohmic nature of the contacts and the operational stability of the sensor are confirmed by the linear I–V characteristics obtained across the tested temperature range as shown in Figure S7 (Supporting Information).

Furthermore, the thermistor sensor device was fabricated by first structuring an open-ended Mo metal layer, following a process analogous to that used for the RTDs. In contrast to RTDs, the metal electrodes in the thermistor design were intentionally left open-ended. The two isolated metal contacts were then bridged by sputtering a temperature-sensitive n-type semiconductor layer, specifically amorphous Indium Gallium Zinc Oxide (a-IGZO), across the entire sensor pattern.The sheet resistance of sputtered a-IGZO layer on the chitosan film showed linear I–V characteristics, and measurements at different locations across the samples indicate sheet resistance values of 354.19 ± 454.33 Ω/sq. Figure S5c,d, Supporting Information. The larger spread observed for the a-IGZO layer is attributed to thickness and microstructural variations inherent to ultra-thin oxide films deposited on flexible polymer substrates. Leaving the contacts open-ended prevents direct current flow through the metal paths, ensuring that temperature-dependent resistance changes arise solely from the semiconductor layer. This configuration enhances sensitivity and preserves the negative temperature coefficient behavior characteristic of thermistors. A schematic of various thermistor designs is presented in Figure 5a. Photographs of the fabricated thermistor sensors are shown in Figure S6f (Supporting Information), while Figure S6g,h (Supporting Information) provide optical micrographs of representative spiral and wavy interdigitated designs, respectively.

The thermistor's performance was evaluated over a temperature range of 25 °C to 55 °C, consistent with the RTD characterization setup. The presented data correspond to a representative thermistor device; heating and cooling curves and the corresponding temperature coefficients for the remaining thermistors are shown in Figure S9b, (Supporting Information), with device-to-device variation. The observed variation is attributed to differences in device geometry, sensor design, and batch-to-batch fabrication, as well as local thickness inhomogeneities associated with the compliant chitosan substrate. The thermal cycle consisted of 5 °C increments held for 20 minutes, with 120-minute stabilization periods before and after the cycle, all maintaining relative humidity below 2%. The relative resistance change during the heating (ramp-up) and cooling (ramp-down) phases is depicted in Figure 5b,c. The sensor exhibited stable response with minimal drift between 25 °C and 35 °C. At temperatures exceeding 35 °C up to 55 °C, an increase in drift was observed, potentially attributable to the differing thermal coefficients of the constituent material layers. The cooling phase demonstrated a more consistent response with negligible drift. A hysteresis of less than ∼0.25 in relative resistance was measured, with the maximum deviation occurring at 25 °C.The thermistor displayed slightly longer thermal kinetics than the RTD, with a response time of ∼20 seconds and a recovery time of ∼30 seconds for thermal steps between 25 °C–30 °C, 30 °C–35 °C and 40 °C–45 °C, highlighting its rapid thermal tracking capability. The calculated temperature coefficient of resistance (α) was 0.0243 $°C^{-1}$ during heating and 0.0126 $°C^{-1}$ during cooling. The obtained TCR value during the heating phase is competitive with, and even exceeds, the typical range reported for state-of-the-art sputtered a-IGZO films (approximately –0.02 $°C^{-1}$), underscoring the high sensitivity of the fabricated device [51, 52].A direct performance comparison against other sensor devices based on materials like transient metals, graphene, and PEDOT:PSS on various natural and synthetic substrates is presented in Table S1 (Supporting Information). The proposed work on a chitosan-based substrate provides an optimal balance of sensitivity, stability in operation, and post-use complete device degradation.

To evaluate stability, resistance measurements were performed at 30 °C, 45 °C, and 55 °C for approximately one hour as shown in Figure 5d. The measured relative resistance values were –0.155±0.006, –0.453±0.020, and –0.629±0.022, respectively. The negative resistance values confirm that the thermistor operates as a negative temperature coefficient (NTC) device, consistent with the n-type semiconductive nature of the a-IGZO layer. Furthermore, Figure 5e displays the multi-cycle testing over five temperature cycles between 25 °C and 55 °C with 30-minute steps. The thermistor demonstrated reliable operation, low hysteresis, a consistent response pattern, and higher sensitivity compared to the RTD.

Leveraging the optical sensitivity of a-IGZO, I–V characteristics were investigated under two conditions: (i) varying illumination wavelengths (400 nm to 900+ nm) at a constant intensity of 150 mW/cm^2 (Figure S10a, Supporting Information), and (ii) varying intensities (50 to 250 mW/cm^2) at a fixed wavelength of 400 nm (Figure S10b, Supporting Information). The results in Figure S10a (Supporting Information) indicates a progressive increase in thermistor resistance as the illumination wavelength shifts from deep blue (400 nm) toward the near-infrared region (>900 nm) at constant intensity. This behavior is attributed to the reduced photon energy at longer wavelengths, which becomes insufficient to generate a substantial population of photo-excited carriers within the a-IGZO layer, thereby lowering its conductivity. Conversely, Figure S10b shows a pronounced decrease in resistance with increasing light intensity (50-250 mW/cm^2) under constant 400 nm excitation. The higher photon flux enhances electronhole pair generation and carrier mobility in the n-type a-IGZO semiconductor, effectively reducing its resistive state. These observations confirm the strong photoresponsive nature of the a-IGZO thermistor and highlight its potential for multifunctional sensing applications where both thermal and optical stimuli can modulate device performance.

The acute contact angle of the chitosan film demonstrates its hydrophilic nature and, consequently, its susceptibility to relative humidity (RH) variations. To evaluate the influence of humidity, both sensors were placed inside a climate chamber while maintaining a constant temperature of 25 °C. The relative humidity

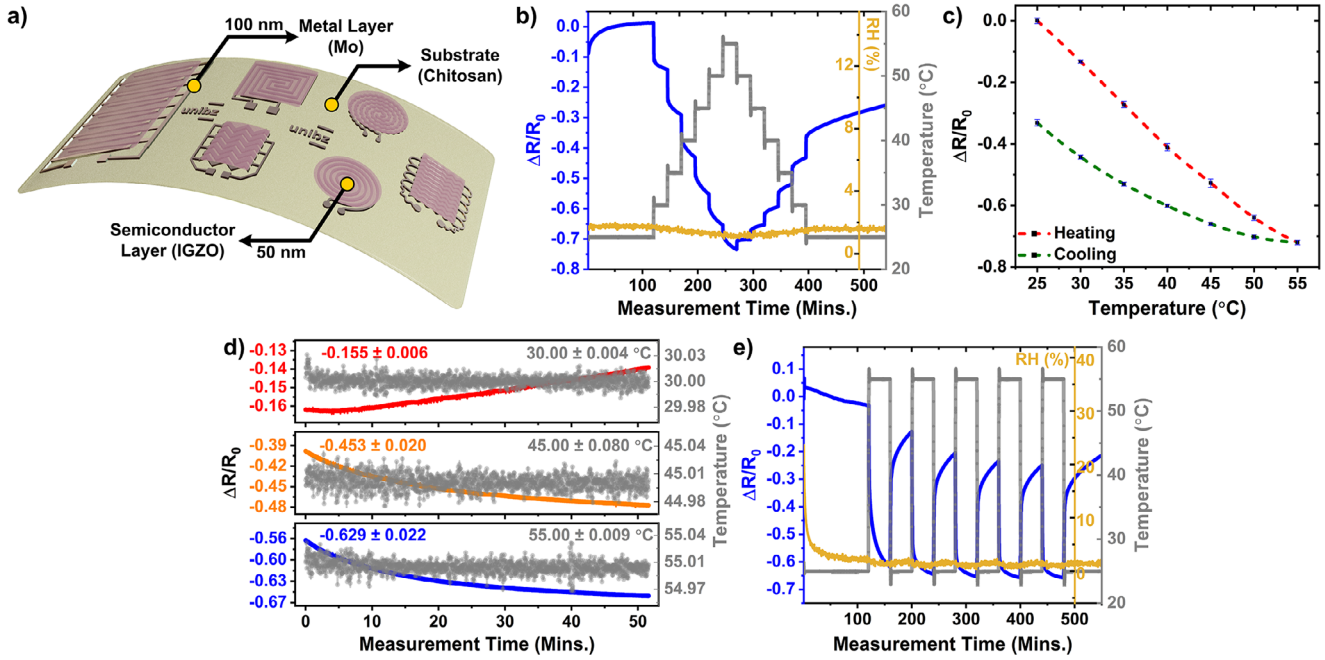

FIGURE 5 | Characterization of Mo-based thermistor (negative temperature coefficient detector) on a chitosan substrate. (a) 2D schematic illustration of the thermistors. (b,c) Relative change in resistance as a function of temperature in a bi-directional sweep between 25 °C and 55 °C. (d) Stability test by monitoring the thermistor response for approximately 1 h at 30 °C, 45 °C, and 55 °C. (e) Cyclic measurements from 25 °C to 55 °C performed five times to evaluate repeatability and device sensitivity.

was initially swept from ~0% to ~50%, and the corresponding sensor responses are shown in Figure S11 (Supporting Information). Figure S11a,c (Supporting Information) presents the ramp-up and ramp-down responses of the RTD and thermistor, respectively. For both sensors, the normalized resistance change increases with increasing RH, indicating a strong humidity-dependent response. The response rises markedly up to approximately 30% RH, beyond which it approaches saturation and exhibits increased variation and instability with further increases in humidity. This saturation behavior suggests that the dominant adsorption sites become progressively occupied at moderate RH levels, thereby limiting further modulation of the sensor resistance. Upon decreasing RH, the response largely recovers toward its initial baseline, with a slight delay attributed to water desorption kinetics. Similarly, Figure S11b,d shows the cyclic responses of the RTD and thermistor, respectively, under repeated RH modulation at a constant temperature of 25 °C. The cyclic measurements exhibit trends consistent with those observed during the ramp-up and ramp-down experiments, with a strong RH-dependent response at low-to-moderate humidity levels followed by saturation at higher RH. This behavior originates from the abundance of hydrophilic functional groups, such as amines and hydroxyls, in chitosan, which readily bind water molecules from the environment.

Based on the observation that the sensor response saturates and becomes unstable beyond ~30% RH in the initial ~0% to ~50% RH sweep (Supporting Information), subsequent measurements were deliberately restricted to the ~0% to ~30% RH range to enable a more detailed and reliable analysis of the humidity response. A series of complementary humidity tests was therefore performed at a constant temperature of 25 °C on both RTDs and thermistors. As shown in Figure 6a,d, the resistance increases monotonically with RH during a controlled ramp from 0% to 30% RH with an average step of 5% RH, confirming a strong and reproducible humidity sensitivity within this range. For the RTD, the increase in resistance is attributed to enhanced carrier scattering and microstrain in the Mo layer induced by water absorption in the chitosan substrate. In the thermistor, humidity-induced surface and interfacial charge effects, amplified by moisture uptake in the hygroscopic substrate, reduce the effective carrier mobility in the a-IGZO layer, resulting in an increase in resistance.

Similarly, cyclic measurements between 5% and 30% RH (Figure 6b,e for the RTD and thermistor, respectively) demonstrate stable and repeatable $\Delta R/R_0$ modulation over multiple humidity cycles. The responses exhibit consistent amplitude and recovery behavior, indicating reversible adsorption–desorption dynamics. In the thermistor, the appearance of a sawtooth-like response during RH stepping reflects finite adsorption and desorption kinetics, where the electrical response does not fully equilibrate within short step times. Increasing the RH dwell time or the post-cycle stabilization period leads to more complete recovery and improved signal stabilization, confirming that the observed behavior is kinetic rather than degradative.

To further assess the robustness of the sensing performance under prolonged exposure, long-term stability tests were conducted at fixed humidity levels of 1%, 15%, and 30% RH for 3 hours each (Figure 6c,f for the RTD and thermistor, respectively). These measurements reveal a stable baseline with minimal signal drift. Collectively, these results demonstrate that the thermal sensors exhibit reliable humidity sensitivity in the low-to-moderate RH regime, governed by adsorption-limited surface interactions, while maintaining excellent reversibility and temporal stability.

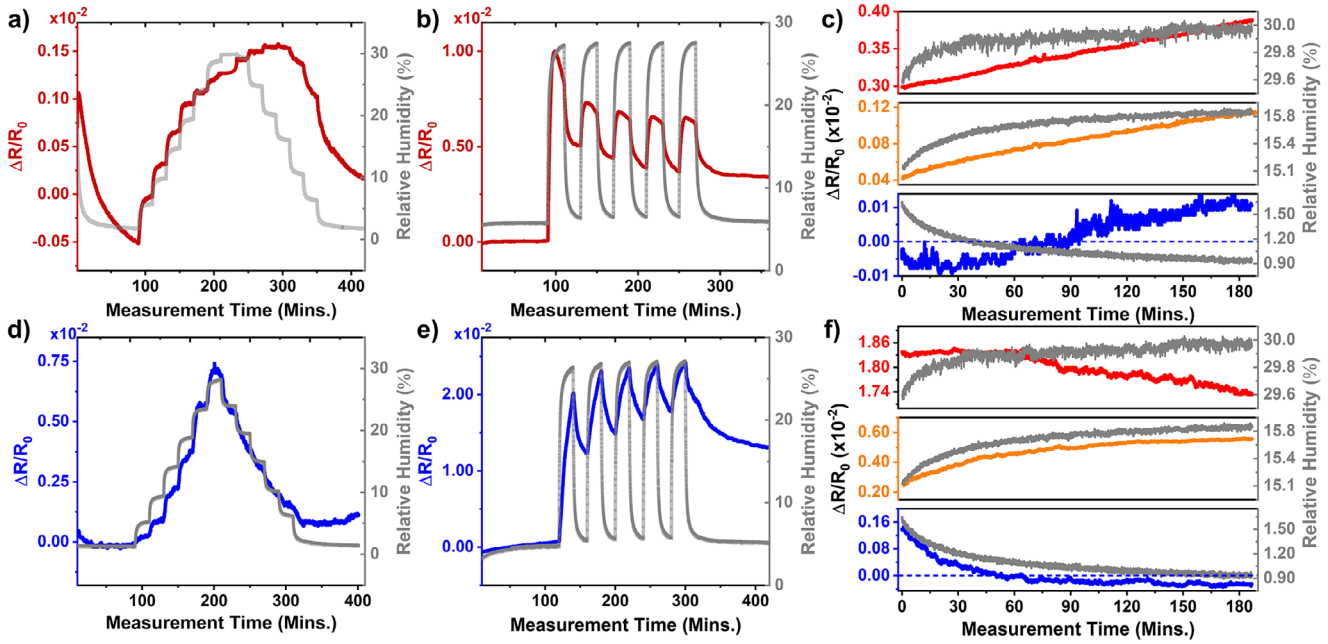

FIGURE 6 | Relative change in resistance ($\Delta R/R_0$) as a function of relative humidity (RH). (a,d) Bi-directional humidity sweeps between ~0% and ~30% RH for the RTD and thermistor, respectively. (b,e) Cyclic humidity response measured between ~5% and ~30% RH over five consecutive cycles to assess device repeatability and sensitivity. (c,f) Long-term stability of the RTD and thermistor evaluated by monitoring the resistance response at fixed humidity levels of 1%, 15%, and 30% RH over approximately 3 hrs.

It is also expected that operation at elevated temperatures would further mitigate humidity-induced effects, as thermally activated desorption and reduced water uptake in chitosan accelerate equilibration and suppress swelling-related resistance drift, thereby improving RH tolerance compared to near-ambient conditions.

The thin-film device architecture ensures not only lightweight construction but also contributes to the favorable thermodynamic and mechanical properties. A key characteristic of such devices is their response to mechanical deformation. To understand the baseline material properties, tensile testing provides insight into the maximum load capacity, Young's modulus, and elongation capability of the chitosan substrate, as shown in Figure S12 (Supporting Information). The pristine chitosan film can withstand a maximum tensile stress of approximately 75 MPa with an elongation of ~10% before rupture, corresponding to a Youngs modulus of ~750 MPa. In comparison, a chitosanglycerol composite exhibits enhanced compliance, showing a lower maximum stress (~63% of the pristine value) and a significantly reduced Youngs modulus of ~40 MPa [25]. The addition of glycerol modifies the stress strain behavior of the film, leading to a more elastomeric response characterized by nonlinear deformation, high strain at low stress, and no distinct yield point [53].

To evaluate mechanical flexibility under practical conditions, the fabricated thermal sensors were bent around cylindrical surfaces with radii ranging from 8 to 16 mm, and their resistance variations were measured.The surface strain was calculated using $\varepsilon = \frac{t}{2r}$, where t is the film thickness and r is the bending radius. Figure 7a shows the normalized resistance change ($\Delta R/R_0$) of the RTD versus bending radius, while Figure 7b shows the same data plotted against the calculated surface strain. Figure 7c,d presents the corresponding results for the thermistor. Both devices exhibited the largest resistance change at the smallest bending radius (8 mm), followed by a gradual return toward the flat-state value as the bending radius increased. Upon re-flattening, the resistance of both devices nearly recovered to their initial value, indicating negligible permanent deformation. Specifically, the RTD showed a maximum normalized resistance variation of ~0.20 at 8 mm, whereas the thermistor exhibited a larger peak variation of ~2.7 under the same condition.This change is attributed to strain-induced effects, such as alterations in carrier mobility, which modify electronic properties. Nevertheless, this similar trend confirms that mechanical deformation has only a minor influence on their electrical characteristics and demonstrates excellent recovery.

In addition to bending, the devices also maintain functionality under more extreme deformations. The mechanical reliability of the device was evaluated by monitoring the normalized resistance change ($\Delta R/R_0$) under twisting)(Figure 7e), crumpling (Figure 7f), and repeated bending stresses. As shown in Figures 7g, minimal resistance variation was observed after twisting ($\Delta R/R_0$<0.1) and after 1000 bending cycles ($\Delta R/R_0 \approx$ 0.2), indicating excellent flexibility and fatigue resistance under torsional and cyclic bending deformations. In contrast, crumpling produced a substantial resistance increase ($\Delta R/R_0 \approx 1.1$), revealing that severe compressive deformation significantly disrupts the conductive pathways. These results highlight the robust mechanical resilience of the sensors, ensuring reliable operation under practical conditions that require conformal or flexible mounting but is susceptible to damage under extreme crumpling, a consideration important for its integration into flexible electronic applications.

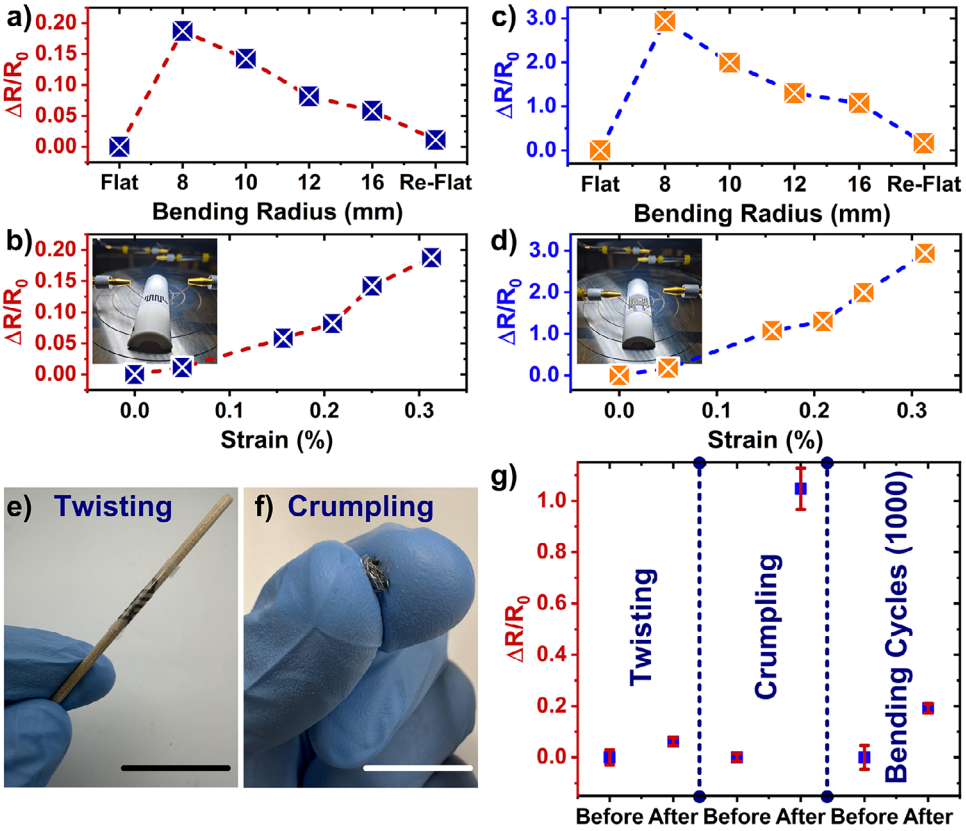

FIGURE 7 | Mechanical performance of the Mo-based RTD and thermistor under various deformation conditions. (a) Relative resistance change ($\Delta R/R_0$) of the RTD under bending radii from 8 to 16 mm, and (b) as function of applied strain, with inset showing the bending setup. (c,d) $\Delta R/R_0$ of the thermistor under the same bending and strain conditions, with inset of its setup. (e,f) Photographs of the devices when twisted around a wooden stick and crumpled (scale bar: 20 mm). (g) Relative resistance change during twisting, crumpling, and cyclic bending for 1000 cycles.

2.3 | Degradation Performance

To assess the transient nature of the devices, in-vitro degradation tests were conducted by immersing the pristine chitosan substrate and fabricated sensors (RTD and thermistor) in three aqueous media at room temperature: deionized (DI) water, an edible lime solution (alkaline), and a vinegar solution (acidic). These conditions were selected to simulate a range of environmental pH levels. The chitosan substrate exhibited rapid and extensive degradation in all media, consistent with its chemical structure. This response is attributed to the intrinsic chemical characteristics of chitosan, a natural polysaccharide composed of repeating 2-acetamido-d-glucose and 2-amino-d-glucose units. The glycosidic linkages connecting these monomeric units are susceptible to hydrolytic cleavage, which facilitates polymer chain scission and the subsequent formation of smaller oligomers. Figure 8 illustrates the degradation progression. Upon immersion, the Mo traces of the devices began to fragment, initiating rapid structural disintegration. The substrate films buckled and curled within the first few hours, except for the samples in vinegar, where the edges were secured with Kapton tape to control the deformation. As the immersion time increased, all films exhibited progressive buckling and deformation, accompanied by a gradual reduction in thickness and optical opacity. Complete dissolution occurred within 50 hours for all samples, with the most rapid degradation observed in the acidic (vinegar) and alkaline (lime) solutions compared to the neutral DI water. The accelerated degradation in the lime and vinegar solutions is attributed to the catalytic effect of both acids and bases on the hydrolysis of glycosidic bonds. The rapid disintegration of the Mo traces indicates a loss of functional sensing capability early in the process, which is a critical aspect of the device's transient nature. Conducting tests across these chemically distinct media provides a robust assessment of the material response under diverse conditions, underscoring the transient characteristics of the chitosan-based platform and sensor devices.

3 | Conclusion

This study presents the design and fabrication of flexible chitosan film-based thin-film thermal sensors, with degradation behavior systematically evaluated as an end-of-life strategy. Scanning electron microscopy (SEM), Fourier-transform infrared spectroscopy (FTIR), UV-Vis spectroscopy, and contact angle measurements confirmed the substrates smooth morphology, characteristic chitosan functional groups, high optical transparency (> 90%) in the visible range, and hydrophilic nature (contact angle ≈ 67°), ensuring compatibility with subsequent device processing. Mo-based RTD sensors and Mo/a-IGZO thermistors were characterized between 25 and 55 °C under controlled humidity. The sensors demonstrated a rapid and reversible response, with their resistance values shifting in direct correlation to temperature changes. The measured temperature coefficients of

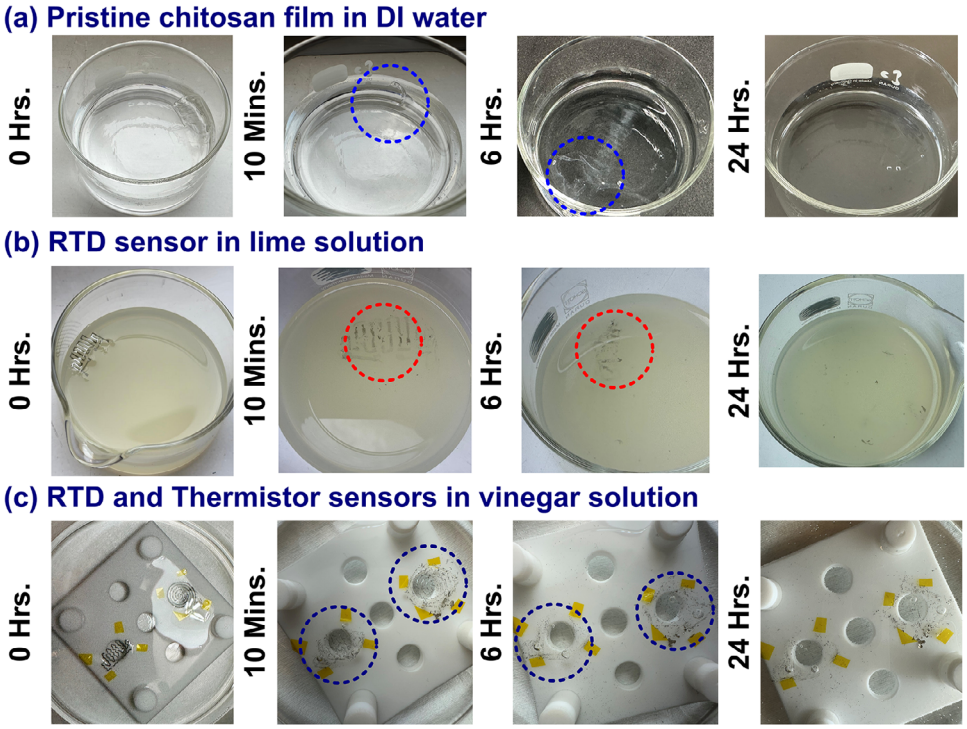

FIGURE 8 | Degradation performance: Photographic images of the degradation performances of the (a) pure chitosan film in DI water, (b) RTD sensor when completely immersed in lime solution and (c) RTD and thermistor sensors while soaked in an edible vinegar solution. Dissolution tests were carried out at room temperature.

resistance (TCR) of 0.001 $°C^{-1}$ and 0.0184 $°C^{-1}$, respectively. These values are slightly lower than the typical 0.0045 $°C^{-1}$ for bulk Mo and comparable to reported 2–5% $°C^{-1}$ for a-IGZO thermistors. The a-IGZO thermistors additionally displayed pronounced light sensitivity, enabling potential multifunctional sensing. Comparative analysis indicates that RTDs offer superior linearity and stability, whereas thermistors provide higher sensitivity and multifunctionality. Immersion tests in deionized water, lime solution, and vinegar demonstrated substantial structural disintegration within 50 h, highlighting the transient nature of the devices. This behavior arises from the intrinsic hydrolyzable glycosidic linkages of chitosan, which could potentially facilitate environmentally conscious and biologically compatible device designs in future studies. Overall, these findings underscore the potential of chitosan-based thin-film thermal sensors as flexible, transient platforms for wearable health monitoring, precision agriculture, and environmental sensing, with prospects for reducing electronic waste and minimizing environmental impact.

4 | Experimental Section

4.1 | Materials

For the preparation of the chitosan solution, CS (High MW, ≥95% deacetylation), acetic acid solution (99 wt.%), and glycerol (MW 92.09 $gmol^{-1}$), were procured from Signa Aldrich. Polyonics XF102 high-performance polyimide (Kapton foil) from Voltera and commercially available 10 cm (L) × 4.5 cm (W) glass slides were used as film carriers. Deionized water was utilized in all experiments.

4.2 | Preparation of Chitosan Films

The solutions of pure chitosan films were prepared by dissolving 250 mg chitosan powder in 25 mL aqueous acetic acid (1% v/v). Continuous magnetic stirring by means of a Branson Digital Sonifier equipped with a 20 kHz horn tip probe was used at 40 °C for 1 hour to obtain homogeneous solutions. Later, the solutions were sonicated in an ultrasound bath for 30 minutes at 45 °C, in order to improve the homogenization. The obtained solutions were dispersed onto the different carriers (Kapton foil and glass wafer) previously placed on the chuck of a film applicator tool (Model: SAFA-219, S.A.M.A. Italia). The films were prepared via the solvent casting method with the automatic applicator, which ensured uniformity, reproducibility, consistency and less defects in the obtained films. The casted films were placed in the fume-hood and allowed to dry at room temperature for 12 hours.

4.3 | Thin Film Fabrication of Thermal Sensors

After preparing the chitosan films, a 100 nm layer of Mo was deposited using a 99.9% pure metallic target in the sputtering tool (Kenosistec, Italy). The deposition was performed at room temperature (~ 25°C) with a DC power of 150 W, under a pressure of 6×10^{-6} bar and an Ar flow rate of 25 sccm, resulting in a deposition rate of 7 nm/min. For the thermistor sensor devices, a 50 nm a-IGZO film was deposited on top of the Mo layer using a target with the composition In:Ga:Zn:O = 1:1:1:4. The deposition was carried out at room temperature (~ 25°C) with a radio frequency (RF) power of 75 W, under a pressure of 2×10^{-6} bar and an Ar flow rate of 25 sccm, resulting in a deposition rate of 1.67 nm/min.

4.4 | Optical and Morphological Characterization of Chitosan Films

The film thickness was measured using a Dektak XT Stylus profilometer. Optical microscopic images of the substrate film were analyzed with a non-contact 3D laser scanning surface profiler (KEYENCE VK-X3000). This profiler captured high-resolution images and provided quantitative measurements to evaluate material deposition and trace patterns. Transmittance spectra were acquired using a Newport Oriel optical measurement system (Irvine, CA, USA). The system included a double-grating monochromator (Oriels Cornerstone), a Newport DET-L-SIUV-R-C Si photodiode, a Stanford SR810, a chopper, and an integrating sphere. The detector and the light source were placed at approximately 90° to avoid directly transmitted light. The hydrophilicity was determined in terms of water contact angle using an Ossila Contact Angle Goniometer (Ossila Ltd., Sheffield, United Kingdom), where water was supplied via a syringe in or out of sessile droplets (~2 μL). A Bruker Invenio Fourier transform infrared (FTIR) spectrometer was used to determine the functional groups of chitosan powder and film, in the range from 400 to 4000 cm^{-1}, by averaging 64 scans at a 2 cm^{-1} wavenumber resolution. Field emission scanning electron microscopy (Thermo Scientific Phenom XL G2 Desktop SEM) was utilized to analyze the surface morphology of the film with an accelerating voltage of 15 kV under different magnifications. Additionally, energy-dispersive X-ray spectroscopy (EDX) was employed for elemental analysis, and surface roughness was assessed to complement the morphological observations.

4.5 | Electrical, Thermal, and Mechanical Characterization of Sensors

The sheet resistance was evaluated using a four-point probe (Ossila) under ambient conditions. Each sheet resistance value (Figure S5, Supporting Information) was collected in three different locations of the test structure and was acquired over multiple measurement instants.

The thermal performance of the fabricated sensor devices was characterized using a custom-designed setup consisting of a sealed chamber, mass flow controllers, a dedicated data acquisition system with a high-performance digital multimeter (Keithley 2000, $6\frac{1}{2}$-digit), a current–voltage source-measure unit (Keithley 2600B Series), and LabVIEW software, maintaining a constant relative humidity below 2%. For heating and cooling cycles, the temperature was swept between 25 °C and 55 °C in 5 °C steps using PID-controlled Peltier modules integrated with PT100 temperature sensors. The electrical contact pads of the sensors were extended using commercial silver conductive paste (RS Pro 123-9911) for external connections.

Bending tests were performed by placing the devices around curved surfaces of various radii and securing them with Kapton tape (Catime 301-10233-01SEA00); current–voltage measurements were carried out using a Keysight B1500A semiconductor parameter analyzer for flat and bent conditions (radii of 8, 10, 12, and 16 mm).

Mechanical durability was evaluated using a custom bending–stretching setup that bent the sensor to 50% of its length for 1000 cycles while monitoring resistance. Illumination effects were characterized by I–V measurements under LED-based source using an Arkeo platform (Cicci Research). Voltage scans were performed in forward and reverse directions at a scan rate of 200 mV s^{-1} with 50 mV steps.

Chitosan film samples were cut with an automatic cutter in rectangular shape, and were subjected to stress–strain testing using an MTS Insight machine fitted with a 100 N load cell. The test was conducted with a gauge length of 20 mm, a sample width of 10 mm, and a crosshead speed of 0.5 mm/s. The Young's modulus (E) was obtained from the slope of the initial linear region of the resulting stress–strain graph.

4.6 | Degradation Process Characterization of Chitosan Films and Sensors

The degradation profile of chitosan-based substrates and fabricated sensors was quantitatively monitored using a customized image acquisition system. This setup, featuring a camera interfaced with an Arduino Uno R3 for automation, captured photographs of the samples (pristine chitosan films, RTDs, and thermistors) at predefined intervals. Each sample had dimensions of 2.5 cm × 2.5 cm. Dissolution tests were performed in three media: deionized (DI) water, an edible lime solution, and a vinegar solution, with a custom 3D-printed PLA holder ensuring stable positioning under magnetic stirring for the vinegar tests.

Acknowledgments

This work is primarily supported by the European Union Next-GenerationEU Progetti Di Ricerca Di Rilevante Interesse Nazionale (PRIN) Bando 2022, grant agreement Prot. 2022L4YZS4.

This research has also been carried out within the PNRR research activities of the consortium iNEST (Interconnected North-East Innovation Ecosystem) funded by the European Union Next-GenerationEU (Piano Nazionale di Ripresa e Resilienza (PNRR) Missione 4 Componente 2, Investimento 1.5 D.D. 1058 23/06/2022, ECS_00000043 Spoke1, RT2 and RT3A, CUP I43C22000250006). This manuscript reflects only the authors' views and opinions, neither the European Union nor the European Commission can be considered responsible for them.

This research was also partially supported by the project PMDI (EFRE1030), cofinanced by the European Union within the Regional Development Fund (ERDF) Programme 2021-2027.

Conflicts of Interest

The authors declare no conflict of interest.

Data Availability Statement

The data that support the findings of this study are available from the corresponding author upon reasonable request.

References

1. O. S. Shittu, I. D. Williams, and P. J. Shaw, "Global E-Waste Management: Can WEEE Make a Difference? A Review of E-Waste Trends, Legislation, Contemporary Issues and Future Challenges," *Waste Management* 120 (2021): 549–563.

2. C. Baldé, R. Kuehr, T. Yamamoto, et al., *The Global E-Waste Monitor 2024* (Geneva/Bonn: International Telecommunication Union (ITU) and United Nations Institute for Training and Research (UNITAR), 2024).

3. M. S. Kim, A. S. Almuslem, W. Babatain, et al., "Beyond Flexible: Unveiling the Next Era of Flexible Electronic Systems," *Advanced Materials* 36, no. 51 (2024): 2406424.

4. Z. Janićijević, T. Huang, D. I. S. Bojórquez, et al., "Design and Development of Transient Sensing Devices for Healthcare Applications," *Advanced Science* 11, no. 20 (2024): 2307232.

5. G. Lee, O. Hossain, S. Jamalzadegan, et al., "Abaxial Leaf Surface-Mounted Multimodal Wearable Sensor for Continuous Plant Physiology Monitoring," *Science Advances* 9, no. 15 (2023): eade2232.

6. M. Wang, Y. Yang, J. Min, et al., "A Wearable Electrochemical Biosensor for the Monitoring of Metabolites and Nutrients," *Nature Biomedical Engineering* 6 (2022): 1225–1235.

7. D. Geng, K. Wang, L. Li, et al., "Thin-Film Transistors for Large-Area Electronics," *Nature Electronics* 6, no. 12 (December 2023): 963–972.

8. A. Rasheed, E. Iranmanesh, W. Li, X. Feng, H. Ou, and K. Wang, "A Wearable Self-Driven Impulse Sensor Based on a Mechanical-Field-Coupled Thin-Film Transistor," *IEEE Electron Device Letters* 39, no. 11 (2018): 1756–1759.

9. G. A. Salvatore, J. Sülzle, F. Dalla Valle, et al., "Biodegradable and Highly Deformable Temperature Sensors for the Internet of Things," *Advanced Functional Materials* 27, no. 35 (2017): 1702390.

10. G. Cantarella, M. Madagalam, I. Merino, et al., "Laser-Induced, Green and Biocompatible Paper-Based Devices for Circular Electronics," *Advanced Functional Materials* 33, no. 17 (2023): 2210422.

11. T. Q. Trung, S. Ramasundaram, B.-U. Hwang, and N.-E. Lee, "An All-Elastomeric Transparent and Stretchable Temperature Sensor for Body-Attachable Wearable Electronics," *Advanced Materials* 28, no. 3 (2016): 502–509.

12. S. Lee, D. Jeong, M. Mativenga, and J. Jang, "Highly Robust Bendable Oxide Thin-Film Transistors on Polyimide Substrates via Mesh and Strip Patterning of Device Layers," *Advanced Functional Materials* 27, no. 29 (2017): 1700437.

13. N. Münzenrieder, D. Karnaushenko, L. Petti, et al., "Entirely Flexible On-Site Conditioned Magnetic Sensorics," *Advanced Electronic Materials* 2, no. 8 (2016): 1600188.

14. H.-R. Kim, M. Furuta, and S.-M. Yoon, "Highly Robust Flexible Vertical-Channel Thin-Film Transistors Using Atomic-Layer-Deposited Oxide Channels and Zeocoat Spacers on Ultrathin Polyimide Substrates," *ACS Applied Electronic Materials* 1, no. 11 (2019): 2363–2370.

15. S. Mao, J. Li, A. Guo, T. Zhao, and J. Zhang, "An Active Multielectrode Array for Collecting Surface Electromyogram Signals Using a-IGZO TFT Technology on Polyimide Substrate," *IEEE Transactions on Electron Devices* 67, no. 4 (2020): 1613–1618.

16. J. H. Kwon, J. Park, M. K. Lee, et al., "Low-Temperature Fabrication of Robust, Transparent, and Flexible Thin-Film Transistors with a Nanolaminated Insulator," *ACS Applied Materials & Interfaces* 10, no. 18 (2018): 15829–15840.

17. J. Zheng, Z. Wang, C. Chen, M. Li, and C. Liu, "A Full-Swing Inverter Based on IGZO TFTs for Flexible Circuits," in *2018 IEEE International Conference on Manipulation, Manufacturing and Measurement on the Nanoscale (3M-NANO)* (2018), 373–376.

18. Z. Zheng, Y. Zeng, R. Yao, et al., "All-Sputtered, Flexible, Bottom-Gate IGZO/Al2O3 Bi-Layer Thin Film Transistors on PEN Fabricated by a Fully Room Temperature Process," *Journal of Materials Chemistry C* 5 (2017): 7043–7050.

19. H.-E. Kim, H.-W. Jang, M. Furuta, J. Yoon, S. Oh, and S.-M. Yoon, "Impact of Organic Inter-Layer Dielectric for Improvement in Mechanical Flexibility of Self-Aligned Coplanar In-Ga-Zn-O Thin-Film Transistor," *Organic Electronics* 96 (2021): 106223.

20. Q. Z. Husain, D. Corsino, S. Krik, A. Stona, N. Münzenrieder, and G. Cantarella, "Investigation of Biodegradable Metals for Green and Sustainable Temperature Sensors," *IEEE Journal on Flexible Electronics* 3, no. 7 (2024): 306–311.

21. D.-H. Kim, Y.-S. Kim, J. Amsden, et al., "Silicon Electronics on Silk as a Path to Bioresorbable, Implantable Devices," *Applied Physics Letters* 95, no. 13 (2009): 133701.

22. A. Carrasco-Pena, F. Catania, M. Haller, M. Nippa, G. Canterella, and N. Münzenrieder, "Flexible Thin-Film Temperature Sensors on Gelatin-Based Biodegradable Substrates for the Development of Green Electronics," in *2023 IEEE International Conference on Flexible and Printable Sensors and Systems (FLEPS)* (2023), 1–4.

23. E. F. Gomez and A. J. Steckl, "Improved Performance of OLEDs on Cellulose/Epoxy Substrate Using Adenine as a Hole Injection Layer," *ACS Photonics* 2, no. 3 (2015): 439–445.

24. Z. Yang, X. Yu, Y. Song, et al., "Flexible and Ultrasensitive Piezoresistive Electronic Skin Based on Chitin/Sulfonated Carbon Nanotube Films," *International Journal of Biological Macromolecules* 259 (2024): 129103.

25. J. Nicoletti, L. Puppulin, J. Routurier, et al., "Enhanced Piezoelectricity in Sustainable-By-Design Chitosan Nanocomposite Soft Thin Films for Green Sensors," *ACS Nano* 19, no. 40 (2025): 35322–35332.

26. M. Dong, A. Soul, Y. Li, et al., "Transient Starch-Based Nanocomposites for Sustainable Electronics and Multifunctional Sensing," *Advanced Functional Materials* 35, no. 1 (2025): 2412138.

27. C. Xu, M. Nasrollahzadeh, M. Selva, Z. Issaabadi, and R. Luque, "Waste-to-Wealth: Biowaste Valorization into Valuable Bio(Nano)Materials," *Chemical Society Reviews* 48 (2019): 4791–4822.

28. T. Maschmeyer, R. Luque, and M. Selva, "Upgrading of Marine (Fish and Crustaceans) Biowaste for High Added-Value Molecules and Bio(Nano)-Materials," *Chemical Society Reviews* 49 (2020): 4527–4563.

29. S. Ngasotter, K. Xavier, M. M. Meitei, et al., "Crustacean Shell Waste Derived Chitin and Chitin Nanomaterials for Application in Agriculture, Food, and Health – A Review," *Carbohydrate Polymer Technologies and Applications* 6 (2023): 100349.

30. E. Commission, "Science Devises Ways to Recycle Crustacean Shells," (2013), https://cordis.europa.eu/article/id/35752-science-devises-ways-to-recycle-crustacean-shells.

31. E. Commission, "Development of an Integrated Biorefinery for Processing Chitin Rich Biowaste to Specialty and Fine Chemicals," (2024), https://cordis.519europa.eu/article/id/35752-science-devises-ways-to-recycle-crustacean-shells.

32. J. L. Shamshina, P. S. Barber, G. Gurau, C. S. Griggs, and R. D. Rogers, "Pulping of Crustacean Waste Using Ionic Liquids: To Extract or Not To Extract," *ACS Sustainable Chemistry & Engineering* 4, no. 11 (2016): 6072–6081.

33. T. Tian, Y. Cai, S. Yang, Y. Guo, and W. Zhou, "Study on Chitosan/Carbon Nanotubes Modified Materials Used to Enhance the Performance of Dental Binder," *Carbon Letters* 33 (2023): 1661–1667.

34. X. Peng, K. Dong, Y. Zhang, et al., "Sweat-Permeable, Biodegradable, Transparent and Self-Powered Chitosan-Based Electronic Skin with Ultrathin Elastic Gold Nanofibers," *Advanced Functional Materials* 32, no. 20 (2022): 2112241.

35. J. Li, Y. Liu, and X. Zhao, "Latest Research Progress on Antibacterial Properties of Chitosan-Based Nanofibers," *Chemical Engineering Journal* 517 (2025): 163776.

36. A. R. Nesic and S. I. Seslija, "19 - The Influence of Nanofillers on Physical–Chemical Properties of Polysaccharide-Based Film Intended for Food Packaging," In *Food Packaging*, ed. A. M. Grumezescu, (Academic Press, 2017), 637–697, https://www.sciencedirect.com/science/article/pii/B9780128043028000194.

37. B. Sultankulov, D. Berillo, K. Sultankulova, T. Tokay, and A. Saparov, "Progress in the Development of Chitosan-Based Biomaterials for Tissue Engineering and Regenerative Medicine," *Biomolecules* 9, no. 9 (2019).

38. G. M. Rani, S. M. Ghoreishian, R. Umapathi, V. Vivekananthan, and Y. S. Huh, "A Biocompatible Triboelectric Nanogenerator-Based Edible Electronic Skin for Morse Code Transmitters and Smart Healthcare Applications," *Nano Energy* 128 (2024): 109899.

39. Y. Chen, M. Ye, L. Song, et al., "Piezoelectric and Photothermal Dual Functional Film for Enhanced Dermal Wound Regeneration via Upregulation of Hsp90 and HIF-1α," *Applied Materials Today* 20 (2020): 100756.

40. S. Lin, C.-C. Chang, and C. Lin, "A Reversible Optical Sensor Based on Chitosan Film for the Selective Detection of Copper Ions," *Biomedical Engineering – Applications, Basis and Communications* 24, no. 5 (2012): 453–459.

41. Y. W. Fen and W. M. M. Yunus, "Utilization of Chitosan-Based Sensor Thin Films for the Detection of Lead Ion by Surface Plasmon Resonance Optical Sensor," *IEEE Sensors Journal* 13, no. 5 (2013): 1413–1418.

42. P. Kumari, A. Kumar, A. Yadav, et al., "Chitosan–Based Highly Sensitive Viable Humidity Sensor for Human Health Monitoring," *ACS Omega* 8, no. 42 (2023): 39511–39522.

43. Y. Su, C. Ma, J. Chen, et al., "Printable, Highly Sensitive Flexible Temperature Sensors for Human Body Temperature Monitoring: A Review," *Nanoscale Research Letters* 15 (2020): 200.

44. M. Ahmed, M. M. Chitteboyina, D. P. Butler, and Z. Celik-Butler, "Temperature Sensor in a Flexible Substrate," *IEEE Sensors Journal* 12, no. 5 (2012): 864–869.

45. *Fundamentals of Piezoelectricity*, Chapter 1, (John Wiley & Sons, Ltd, 2021), 1–18.

46. M. Saadi, M. Erouel, A. Tall, et al., "Morphological, Optical, and Dielectric Properties of Chitosan Biopolymer Thin Films Synthesized by Spray Pyrolysis," *ACS Omega* 10, no. 40 (2025): 46384–46392.

47. J. Jyotish, R. Nayak, S. Moharana, and R. N. Mahaling, "Enhanced Dielectric and Electrical Studies of Carboxyl Functionalized Multiwalled Carbon Nanotube-Based Chitosan/PEG-CeO_2 Composite Films," *Journal of Materials Science: Materials in Electronics* 36, no. 21 (2025): 1360.

48. M. Rinaudo, "Chitin and Chitosan: Properties and Applications," *Progress in Polymer Science* 31, no. 7 (2006): 603–632.

49. M. Dash, F. Chiellini, R. M. Ottenbrite, and E. Chiellini, "Chitosan—A Versatile Semi-Synthetic Polymer in Biomedical Applications," *Progress in Polymer Science* 36, no. 8 (2011): 981–1014.

50. A. Sionkowska, "Current Research on the Blends of Natural and Synthetic Polymers as New Biomaterials," *Progress in Polymer Science* 36, no. 9 (2011): 1254–1276.

51. Y. Wang, J. Chen, Y. Zhou, et al., "Thermal Sensitivity of Amorphous In-Ga-Zn-O Thin Film Transistors for Temperature Sensor Applications," *Applied Physics Letters* 105, no. 14 (2014): 143501.

52. H. Hosono, M. Yasukawa, and H. Kawazoe, "Exploring Electro-chemistry and Thermal Stability of Amorphous Oxide Semiconductors," *Journal of Non-Crystalline Solids* 354, no. 19-25 (2008): 2796–2800.

53. W. D. Callister and D. G. Rethwisch, *Fundamentals of Materials Science and Engineering: An Integrated Approach*, 5th edition (Hoboken, NJ: Wiley, 2020).

Supporting Information

Additional supporting information can be found online in the Supporting Information section.

Supporting File: aelm70302-sup-0001-SuppMat.pdf.